Article

Nickel-Based Single-Atom Alloys for Methane Dehydrogenation and the Effect of Subsurface Carbon: First-Principles Investigations

Naiyuan Dong [1,2], Tanglaw Roman [3,4] and Catherine Stampfl [1,2,*]

1 School of Physics, The University of Sydney, Sydney, NSW 2006, Australia; ndon5992@uni.sydney.edu.au
2 The University of Sydney Nano Institute, The University of Sydney, Sydney, NSW 2006, Australia
3 Flinders Institute for Nanoscale Science and Technology, College of Science Engineering, Flinders University, Bedford Park, SA 5042, Australia; tanglaw.roman@flinders.edu.au
4 Flinders Microscopy and Microanalysis, Flinders University, Bedford Park, SA 5042, Australia
* Correspondence: catherine.stampfl@sydney.edu.au

Abstract: Using ab initio calculations, the reaction path for methane dehydrogenation over a series of Ni-based single-atom alloys (Cu, Fe, Pt, Pd, Zn, Al) and the effect that subsurface carbon at the Ni(111) surface has on the reaction barriers are investigated. Due to the well-known problem of coking for Ni-based catalysts, the adsorption and associated physical properties of 0.25 ML, 1.0 ML, and 2 ML of carbon on the Ni(111) surface of various sites are first studied. It is found that the presence of subsurface carbon reduces the stability of the intermediates and increases the reaction barriers, thus reducing the performance of the Ni(111) catalyst. The presence of Al, Zn, and Pt is found to reduce the barriers for the $CH_4 \rightarrow CH_3 + H$ and $CH_3 \rightarrow CH_2 + H$ (Pt); and $CH \rightarrow C + H$ (Al, Zn) reactions, while Ni(111) yields the lowest barriers for the $CH_2 \rightarrow CH + H$ reaction. These results thus suggest that doping the Ni surface with both Al or Zn atoms and Pt atoms, functioning as distinct active sites, may bring about an improved reactivity and/or selectivity for methane decomposition. Furthermore, the results show that there can be significant adparticle–adparticle interactions in the simulation cell, which affect the reaction energy diagram and thus highlight the importance of ensuring a common reference energy for all steps.

Keywords: density functional theory; single-atom alloys; methane reduction

1. Introduction

Reforming abundant natural gas into useful fuels and chemicals is an enormously important technological process. A significant proportion of the world's hydrogen is made through natural gas reforming. Natural gas contains methane, which is used to produce hydrogen through thermal processes, such as steam methane reforming or partial oxidation. Hydrogen production via methane has the advantage of extensive and well-developed extraction, storage, and distribution structures already in place [1,2]. Methane is a stable molecule with strong bonding between the carbon and hydrogen atoms, and therefore the key problem lies in how to lower the reaction energy barrier. For current progress in methane decomposition, we refer to a recent review [3].

The steam reforming of methane involves high temperatures (700–1000 °C) and high pressures of steam (H_2O) ≈ 3–25 bar, where the main products are hydrogen and carbon monoxide. Subsequently, via the water–gas shift reaction, the carbon monoxide and steam are reacted together using a catalyst to produce carbon dioxide and more hydrogen. Steam reforming is endothermic, and heat must be supplied to the process for the reaction to proceed. Thus, the cost–benefit of this reaction has been questioned [4]. In the partial oxidation reaction, methane reacts with a limited amount of oxygen that is not enough to completely oxidize the hydrocarbons to carbon dioxide and water. Because there is less than

the stoichiometric amount of oxygen, the reaction products primarily contain hydrogen and carbon monoxide. Again, via the water–gas shift reaction, the carbon monoxide reacts with water to form carbon dioxide and more hydrogen. In contrast, partial oxidation is an exothermic process, giving off heat.

Recently, dry reforming of methane (DRM) has attracted significant attention because it provides a promising method for synthesizing CO and hydrogen, converting two greenhouse gases, CO_2 and CH_4, into valuable sources of fuels and chemicals. Minh et al. have compared and reviewed the possible methods for generating hydrogen through biogas reforming with steam reforming (SRM), dry reforming (DRM), dual reforming, and tri-reforming of methane, where it was found that SRM and DRM are the most promising and practical methods [5]. It was concluded that the main obstacle to putting DRM into practical application is to find approaches that can counter the high activation and reaction barriers of CO_2 and CH_4 dissociation. The key to this is developing new materials that will efficiently and selectively catalyze the necessary reactions and be stable under the reaction conditions.

The DRM reaction is endothermic and requires high temperatures. Metals, such as Pd and Pt, show excellent catalytic performance and minimize the build-up of excessive carbon at the surface, which deactivates the catalyst. However, application of these noble metals in large-scale processing is limited by their high cost and low availability. Therefore, transition metals, such as nickel used in nickel-based catalysts, are a promising alternative as they have comparable catalytic properties. The main disadvantage is that they are more susceptible to sintering and deactivation due to build-up of carbonaceous deposits, i.e., coke formation. The exploration and identification of new nickel-based catalysts that reduce these two negative effects are intense areas of current research. Some approaches include the introduction of supports, such as mesoporous structures, due to their high specific surface area and large pore size. In these structures, there is a strong Ni–support interaction that helps to stabilize the catalyst and increase the dispersion of the Ni particles [6]. Adding promoters (dopant atoms) to Ni-based catalysts is another avenue to enhance the catalytic activity, stability, and coking resistance, such as alkaline earth metal oxides [7], as well as novel single-atom alloys (SAAs) [8,9]. Alloying different metal atoms into the surface of another provides a way to tune the electronic structure of the surface and hence tailor its performance. In particular, SAAs [10] have demonstrated enhanced properties, e.g., in reducing CO poisoning [11] and selective heterogeneous hydrogenations [12].

The recognition of using fossil fuels, such as methane, to generate hydrogen as a promising and reliable method has led to intense research into the methane decomposition reaction [1] because irrespective of which of the reactions discussed above is considered, utilizing methane to synthesize a target product involves the crucial steps of the dehydrogenation of methane [13]. As mentioned above, the development of new catalysts that afford the efficient transformation of methane [14] is of high current importance.

In the present work, we investigate a series of Ni-based SAAs for methane decomposition using first-principles calculations. Our strategy is to investigate a range of metal dopants with different characteristics, from platinum-group metals with partially filled d-bands to those with full *d*-states, as well as those that form magnetic elements and, finally, free electron metals. In this way, we aim to identify what electronic nature of the doped atoms yields improved performance for the various reaction steps involved in the dehydrogenation of methane. We start by investigating the adsorption of carbon atoms on and under the Ni(111) surface due to its role in coking. Subsequently, we investigate the adsorption of methane, hydrogen, and the CH_3, CH_2, and CH intermediates on the Ni(111) surface, the Ni(111) surface with subsurface carbon atoms, and a series of SAA alloy surfaces, identifying the most favourable sites and associated adsorption energies. We then calculate the reaction pathways and activation barriers for methane dehydrogenation over these surfaces to compare the relative catalytic performance.

From our results, we find that except for graphene formation at the surface, subsurface adsorption of carbon atoms is preferred over on-surface adsorption, and the presence of

such carbon atoms under the surface has a detrimental effect on methane decomposition. In contrast, Al-, Zn-, and Pt-SAA surfaces lower certain reaction barriers and could bring about an improvement in methane dehydrogenation compared to the pure Ni(111) surface.

2. Calculation Method

The density-functional theory (DFT) calculations are performed using VASP (the Vienna Ab initio Simulation Package) [15] with the generalized gradient approximation (GGA) of Perdew, Burke, and Ernzerhof (PBE) [16] for the exchange-correlation functional, and van der Waals (vdW) interactions are included using the D3 correction [17]. The energy cut-off is taken to be 450 eV for all calculations, which is selected based on the results of convergence tests (cf. Figures S1–S4 of the supplementary information (SI)). The atomic structure is optimized until the forces on all of the relaxed atoms are less than 0.01 eV/Å. The calculations are performed, including spin-polarization.

We use a five-layered Ni(111) surface with a (4 × 4) surface unit cell and adsorb the reactants on one side of the slab, where the bottom two atomic layers are held fixed at their bulk-like positions. The vacuum region is taken to be 15 Å, and the **k**-point mesh is 3 × 3, using the Monkhorst–Pack method for Brillouin zone integration [18]. For all surface calculations, the dipole correction to the total energy is included, which reduces the interactions of the repeated slabs across the vacuum region.

The nudged elastic band (NEB) method and the VASP TST (transition state tools, VTST) are used [19,20] to calculate the transition states and associated reaction energy barriers and minimum energy pathways. In VTST, the climbing image method [19] is employed to generate the highest barrier energy image at the saddle point automatically, other than giving the two nearest energy points about the saddle point. This climbing method moves the highest energy to the saddle point, which simplifies the calculation process.

The adsorption energy of different atoms and molecules on the surface is calculated as:

$$E_{ads} = \frac{1}{n}(E_{tot} - E_{clean} - nE_{free}) \tag{1}$$

where E_{tot} represents the total energy of the adsorption system, E_{clean} is the total energy of the clean surface, and E_{free} is the total energy of the free, isolated atom or molecule. n is the number of atoms or molecules adsorbed on the surface in the surface unit cell. Thus, a negative value represents an exothermic adsorption energy.

The work function, Φ, is the lowest energy required to remove an electron from the surface, and it is given by:

$$\Phi = E_{vac} - E_f \tag{2}$$

where E_{vac} is the vacuum energy and E_f is the Fermi. These energies are obtained from plots of the (x, y)-averaged electrostatic potential as a function of z, the direction perpendicular to the surface. An example is shown in Figure S5 for the clean Ni(111) surface and with 1 ML of subsurface carbon atoms.

We define the contraction/expansion between the surface layers as:

$$\Delta d_{ij} = \frac{d_{ij} - d_0}{d_0} \times 100\% \tag{3}$$

where Δd_{ij} is the percentage of inward/outward relaxation between the ith and jth layer, d_{ij} represents the corresponding average interlayer spacing along the z-direction, and d_0 is the interlayer spacing of the ideal clean Ni(111) surface.

3. Results: Carbon Adsorption on Ni(111)

The lattice parameter of bulk nickel is calculated to be 3.524 Å. This is in excellent agreement with the experimental result of 3.52 Å [21] and also with recent first-principles calculations, e.g., 3.506 Å and 3.52 Å, as reported in Refs. [22,23], respectively. The calculated cohesive energy is 4.88 eV, which is in excellent agreement with previous first-principles cal-

culations using the GGA, namely 4.87 eV [24], and in good agreement with the experimental value of 4.44 eV [25].

3.1. Adsorption of Carbon on Ni(111): 0.25 and 1 ML

We first investigate the adsorption of carbon atoms on the Ni(111) surface for coverages of 0.25 and 1.0 monolayers (ML). First, 1 ML is determined to have the same number of adsorbates as there are nickel atoms in the (111) layer. We consider five different sites, as shown in Figure 1, namely, on-top, bridge, fcc-hollow, hcp-hollow, and the subsurface octahedral site. The resulting adsorption energies, C-Ni bond-lengths, and the change in the first interlayer spacings with respect to the corresponding bulk (111) spacing are listed in Table 1. It can be seen that for all sites, the lower coverage for 0.25 ML has a greater adsorption energy than for 1 ML. Further, it is found that the subsurface fcc site is the most favourable for both 0.25 ML and 1.0 ML, with values of −7.38 eV and −6.29 eV, respectively. Subsurface adsorption induces a significant expansion of the first interlayer spacing of 7.8% and 24.1% for these respective coverages. The next most favourable site is the hcp-hollow site for 0.25 ML, which is just 0.07 eV more favourable than the fcc-hollow site, with values of −6.95 eV and −6.88 eV, respectively. For 1.0 ML, the situation is the opposite, with the fcc-hollow slightly more favourable than the hcp-hollow site, with values of −5.10 eV and −5.08 eV, respectively; however, this is a difference of just 0.02 eV. For 0.25 ML, the more favourable energy of the hcp-hollow may be related to the fact that it induces a smaller expansion of the first interlayer spacing (≈1.4%) than the fcc-hollow site (≈3.3%). For 1.0 ML, the expansion of the first interlayer spacing is similar for the hcp (≈5.6%) and fcc (≈6.2%) sites, varying by just 0.6%. For both coverages, the site with the greater adsorption energy has a (slightly) shorter C-Ni bond-length, as may be expected. The C-Ni bond-length is slightly longer for the 1 ML structures, consistent with the weaker adsorption energies. The reduced adsorption energy for the 1 ML structures reflects the repulsive interactions between the C atoms, which are partially negatively charged [26], which is in line with the difference in electronegativities of C (2.55) and Ni (1.91).
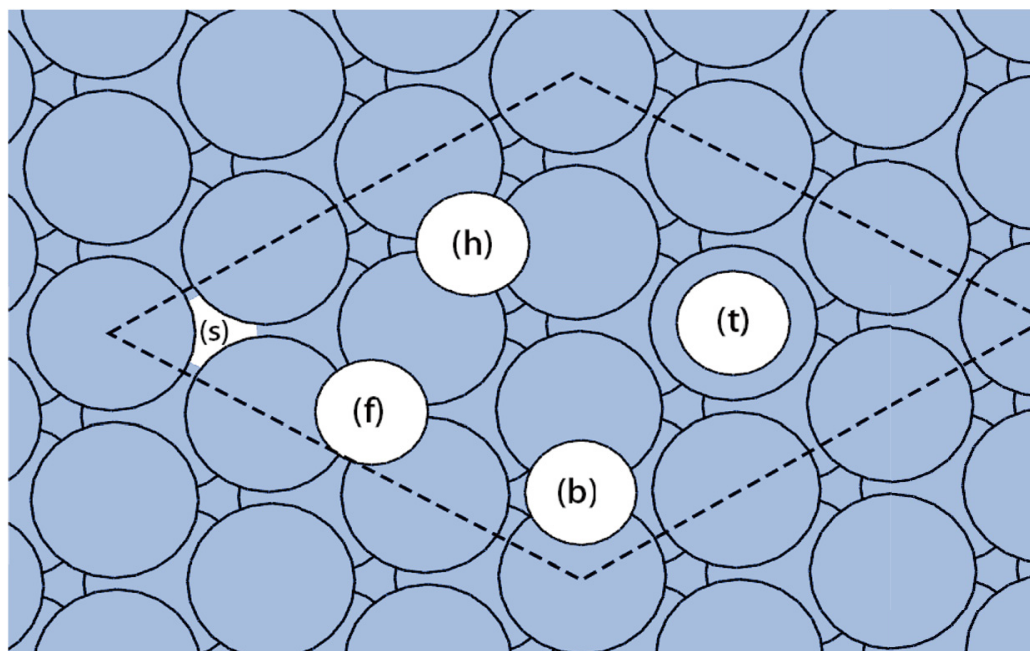

Figure 1. Different adsorption sites for a carbon atom on the Ni(111) surface: (t,b,f,h,s), representing on-top, bridge, fcc-hollow, hcp-hollow, and subsurface octahedral hollow sites, respectively.

Table 1. Calculated adsorption energies, E_{ad}, C-Ni bond lengths, R, change in the first layer spacings, Δd_{12}, expressed as a percentage change with respect to the ideal layer spacing, d_0, of the clean (111) surface, work function, Φ, and work function change, $\Delta\Phi$, with respect to the clean Ni(111) surface (which has $\Phi = 5.04$ eV) for coverages, $\Theta = 0.25$ ML, and 1 ML. These results are obtained without vdW corrections and using a (4 × 4) surface unit cell.

Θ (ML)	SITE	E_{ad} (eV)	R (Å)	Δd_{12} (%d_0)	Φ (eV)	$\Delta\Phi$ (eV)
1	top	−4.46	1.17	4.56	7.06	2.02
1	bridge	−4.77	1.84	4.64	7.26	2.22
1	fcc	−5.10	1.86	6.17	6.80	1.77
1	hcp	−5.08	1.87	5.64	6.92	1.88
1	subsurface	−6.29	1.92, 1.93	24.12	5.14	0.10
0.25	op	−4.55	1.64	2.12	6.03	0.99
0.25	bridge	−6.47	1.72	6.73	5.87	0.84
0.25	fcc	−6.88	1.77	3.25	6.07	1.03
0.25	hcp	−6.95	1.77	1.41	5.92	0.88
0.25	subsurface	−7.38	1.84, 1.87	7.79	5.31	0.27

The calculated adsorption energies can be compared with previous results reported in the literature. For example, Zhang et al. [27], using VASP with the GGA functional, studied the adsorption of a carbon atom on the Ni(111) surface in a (6 × 6) surface unit cell and found the hcp-hollow site to be favourable with an adsorption energy of −7.25 eV, and the 0.07 eV more favourable than the fcc site, consistent with the present results (the subsurface site was not considered). The adsorption energy values in the work of Zhang et al. are, however, about 0.3 eV larger, possibly due to the fact that they only used two layers to simulate the Ni(111) surface. Klinke et al. [26], using the FP-LAPW method and the GGA, also found that the subsurface site was most favourable for the 0.25 ML and 1 ML coverages; it was more favourable by 0.62 eV and 1.09 eV than the next most favourable site, respectively. This is close to the present analogous values of 0.43 eV and 1.19 eV. One difference is that for 0.25 ML, Klinke et al. found the fcc-hollow site to be more favourable than the hcp-hollow site (by 0.71 eV). The reason for this difference is unclear. For 1 ML, the adsorption energy of the fcc- and hcp-hollow sites were found to be identical, consistent with the present results. The study by Cinquini et al., using VASP and the GGA functional, found for 0.25 ML coverage that the subsurface octahedral site was most favourable (−7.39 eV), followed by the hcp-hollow site (−6.97 eV) and then the fcc-hollow site (6.93 eV), in close agreement with the present values.

To gain insight into the bonding mechanism of C on Ni(111), we calculate the work-function and partial density-of-states (PDOS). The calculated work function, Φ, for each of the considered sites and coverages as well as the change in work function with respect to that of the clean Ni(111) surface, $\Delta\Phi$, are listed in Table 1. The value of the work function for the clean Ni(111) surface is 5.04 eV. The corresponding experimental value of the work function is 5.35 eV from the CRC Handbook [28], while Michaelson [29] concluded from experimental studies that the work function of clean Ni(111) is 5.15 eV. Thus, the theoretical value is slightly underestimated compared to the experiment.

From Table 1, it can be seen that the adsorption of C on the Ni(111) surface results in a notable increase in the work function; namely, for the favourable on-surface sites at 0.25 ML and 1.0 ML, it increases by 0.88 eV and 1.77 eV, respectively. This is due to the transfer of electron density from the Ni surface to the adsorbed C atom, giving rise to a surface dipole moment that increases the energy required to remove an electron from the Fermi level to the vacuum. The work function change for the subsurface site is notably smaller at 0.27 eV and 0.10 eV for 0.25 ML and 1.0 ML, respectively, due to the formation of dipoles with directions opposing each other (negative on the C atom and positive on the Ni atoms above and below). A similar increase in work function occurs for other strongly electronegative adsorbates, e.g., for oxygen on gold [30] and nitrogen on copper [31], and, correspondingly, a decrease occurs for electropositive adsorbates [32].

In Figure 2, the partial density-of-states (PDOS) for the adsorption of C on Ni(111) is shown for the fcc-hollow surface and the subsurface site for 1 ML coverage. The PDOS illustrate the bonding character between the carbon atoms and the nickel surface. For strong metal–adsorbate bonding, the antibonding electronic states are mostly found above the Fermi level. As shown in Figure 2, the carbon atom $2p_{x+y}$ orbitals for both the fcc-hollow site and the subsurface site have peaks at roughly −4 eV and 4 eV, which correspond to the adsorbate–surface bonding and antibonding states, respectively. For the carbon atoms in the fcc-hollow site, the PDOS of the carbon $2s$ and carbon $2p_z$ states at −10 eV exhibit an *sp* orbital hybridization and interaction with the Ni surface.
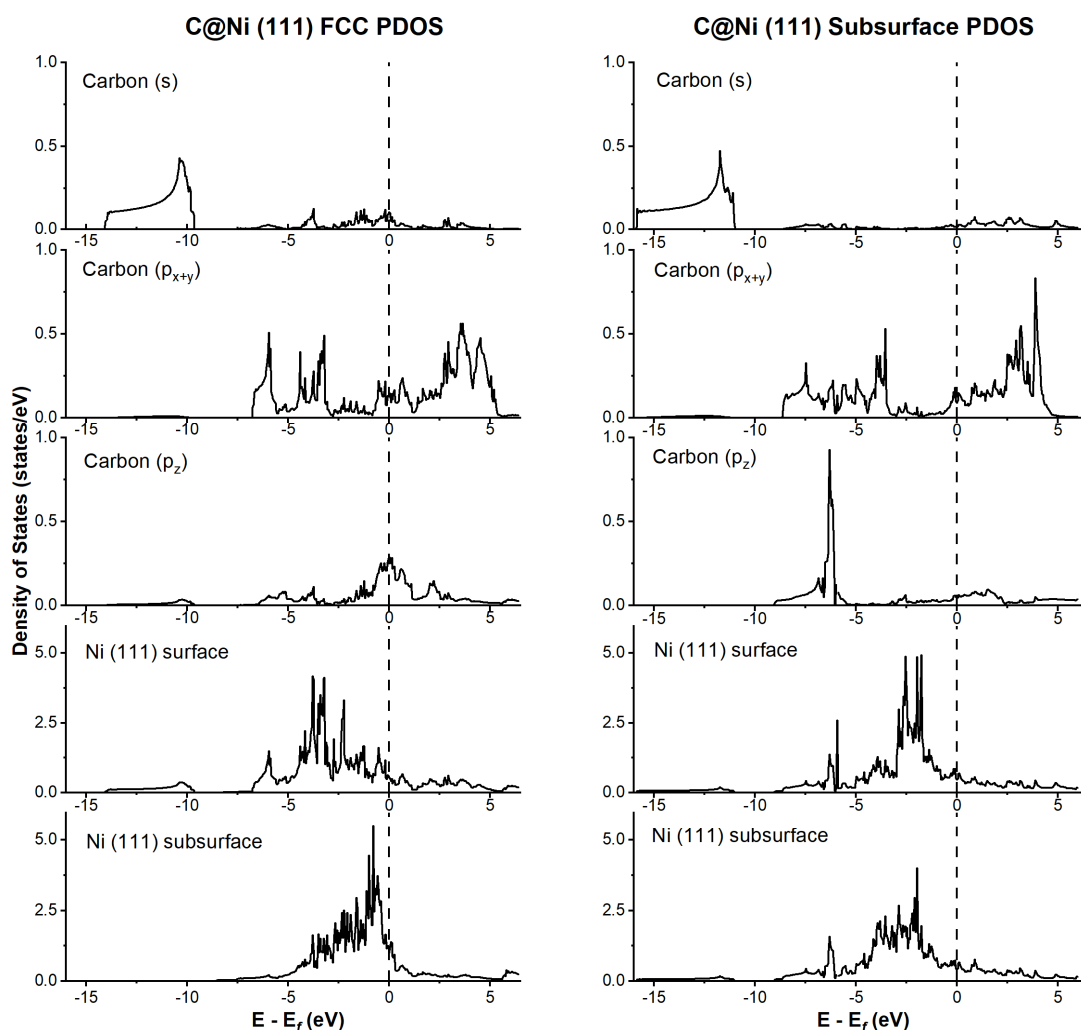

Figure 2. PDOS for a carbon atom (1.0 ML) adsorbed on the fcc-hollow (**left**) and subsurface octahedral (**right**) sites of Ni(111). The energy zero is at the Fermi level, indicated by the dashed line.

For carbon in the subsurface site, as shown in Figure 2 (right), a peak due to the carbon $2p_z$ orbital is observed at −6 eV, which is hybridized with the Ni layers above and below it. It can also be seen that the peaks of the Ni(111) subsurface layer are notably lower at the Fermi level than for the on-surface case. The main noticeable difference between surface and subsurface adsorption is the reduction in the C-p_z states at the Fermi level for the subsurface case.

3.2. ML Hexagonal Structures of C on Ni(111) and vdW Corrections

Experimentally, for coverages of C on Ni(111) higher than 0.45 ML, it has been reported that reconstruction occurs [33,34], while above 700 K, graphitic carbon forms [33].

In the following, we consider a layer of graphene (2 ML) on Ni(111), where due to the close lattice mismatch this results in a tensile strain of only 1.3%. Several possible lateral configurations are considered, as shown in Figure 3, namely, fcc-top, hcp-top, fcc-hcp, and bridge-top. Because the 2 ML graphene-like adsorption structures are expected to be very weakly bound, van der Waals interactions may play a more significant role; this will also be important for the study of the dehydrogenation of methane due to the weak bonding of methane to the surface. We consider two different vdW-corrections, namely, the DFT-D3 method (Becke–Johnson damping) [17,35] and the vdW-DF functional of Langreth and Lundqvist, the so-called optB86b- vdW functional [36]. The results are listed in Table 2. The adsorption energy is also given with respect to a graphene layer, i.e., $E_{ad} = 1/n \, (E_{tot} - E_{clean} - nE_{graphene})$, where $E_{graphene}$ is the total energy of a C atom in graphene.
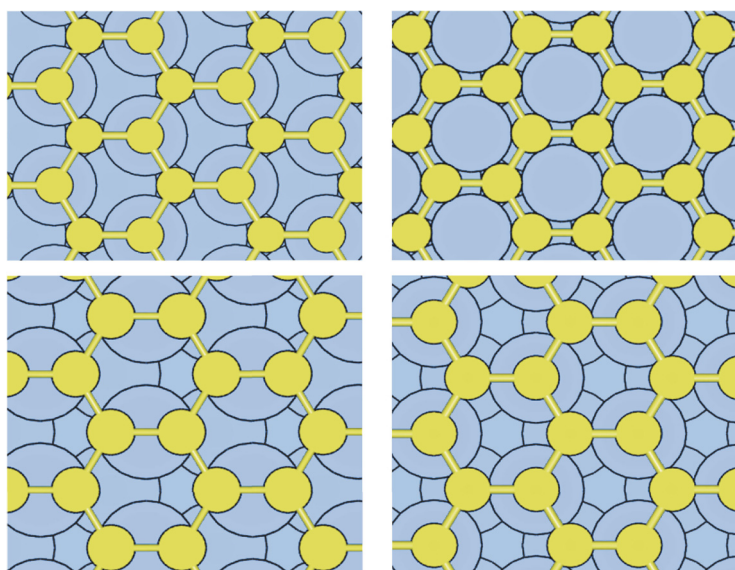

Figure 3. The 2 ML coverage of carbon atoms (yellow) in the fcc-top (**upper left**), fcc-hcp (**upper right**), bridge-top (**lower left**), and hcp-top (**lower right**) sites on Ni(111).

We also consider the lower-coverage (0.25 ML and 1 ML) structures discussed above using both approaches to determine how significant the effect is. We find that both vdW correction approaches predict the same preferred adsorption site for the 0.25 ML and 1 ML structures as when not including vdW corrections. Interestingly, for the 2 ML structures, without including vdW corrections, the adsorption of all considered structures is endothermic when calculated with respect to graphene, as indicated by the positive adsorption energies, with the most favourable being the fcc-top structure. For both vdW corrections, the resulting adsorption energy becomes exothermic, strengthening the adsorption energy by 0.1–0.25 eV. For the D3, the favoured structure is the fcc-top (by only 0.01 eV), while for the optB86b-vdW, the bridge-top structure is most favourable (by only 0.01 eV); thus, both structures are practically degenerate.

For the optB86-vdW method, the average energy difference ΔE (relative to no correction included) for 0.25 ML, 1 ML, and 2 ML is −0.19 eV, −0.24 eV, and −0.25 eV, respectively. For the DFT-D3 method, the analogous values are −0.19 eV, −0.25 eV, and −0.10 eV, respectively. For the 2 ML graphene structure, comparing the energy difference ΔE between the adsorption energies with and without vdW corrections, it can be seen from Table 2 that the opt86b-vdW method yields a slightly more stable interaction between the C-layer and the substrate, but both vdW corrections yield very similar results. In our subsequent investigations of methane dehydrogenation, the DFT-D3 approach is used.

Table 2. For 0.25 ML, 1 ML, and 2 ML coverage. For the 2 ML structures, the second value is the adsorption energy calculated with respect to the total energy of a C atom in graphene (rather than a free C atom). The corresponding values for no vdW correction are also listed, along with the change in energy, ΔE, due to including the vdW correction.

Method	Coverage (ML)	Site	E_{ads} (eV)	E_{ads} (eV) no vdW	ΔE (eV)
	0.25	on-top	−4.76	−4.55	−0.22
	0.25	bridge	−6.64	−6.47	−0.17
	0.25	fcc	−7.08	−6.88	−0.20
	0.25	hcp	−7.15	−6.95	−0.20
	1	on-top	−4.70	−4.46	−0.24
	1	bridge	−5.03	−4.77	−0.26
optB86b-vdW	1	fcc	−5.35	−5.10	−0.24
	1	hcp	−5.34	−5.08	−0.26
	1	subsurface	−6.05	−5.86	−0.19
	2	bridge-top	−8.17, −0.26	−7.91, 0.04	−0.30
	2	fcc-top	−8.07, −0.15	−7.92, 0.03	−0.18
	2	hcp-top	−8.15, −0.24	−7.91, 0.04	−0.28
	0.25	on-top	−4.78	−4.55	−0.23
	0.25	bridge	−6.62	−6.47	−0.15
	0.25	fcc	−7.06	−6.88	−0.18
	0.25	hcp	−7.13	−6.95	−0.18
	1	on-top	−4.73	−4.46	−0.27
	1	bridge	−5.02	−4.77	−0.25
DFT-D3	1	fcc	−5.35	−5.10	−0.25
	1	hcp	−5.33	−5.08	−0.25
	1	subsurface	−6.08	−5.86	−0.22
	2	bridge-top	−7.97, −0.06	−7.91, 0.04	−0.10
	2	fcc-top	−7.98, −0.07	−7.92, 0.03	−0.10
	2	hcp-top	−7.96, −0.05	−7.91, 0.04	−0.10

4. Results: Adsorption of Methane and Intermediates

Before investigating the minimum energy reaction pathways and associated energies for methane dehydrogenation, it is necessary to determine the favourable adsorption sites and associated adsorption energies of all of the reaction intermediates and products, i.e., $CH_x(x = 1, 4)$ fragments, C and H on the Ni(111) surface, with and without subsurface C, and on the SAA surfaces.

4.1. Adsorption on Ni(111) and $C_{subsurf}$/Ni(111)

Due to the stable tetrahedral bonding of methane, the binding of methane on Ni(111) is very weak. Different adsorption sites for methane adsorption are tested to determine the most favourable configuration, as shown in Figure 4. Specifically, the adsorption sites considered are on-top, bridge, fcc-, and hcp-hollow sites, where the most favourable site is the on-top site, with an adsorption energy of −0.15 eV. The obtained adsorption energies are listed in Table 3. This finding can be compared with the earlier ab initio calculations of Zhu et al., who obtained −0.02 eV, and with Niu et al. [37], who obtained −0.035 eV. The former study also used the VASP code with the GGA-PBE functional, but it did not include van der Waals corrections, and it used a smaller slab (four layers) and a smaller surface unit cell (3 × 3). The latter study used the CASTEP code with the same functional and a smaller surface unit cell of (2 × 2) and four layers, and it also did not include vdW corrections. The latter point may account for the weaker binding found in these two studies.
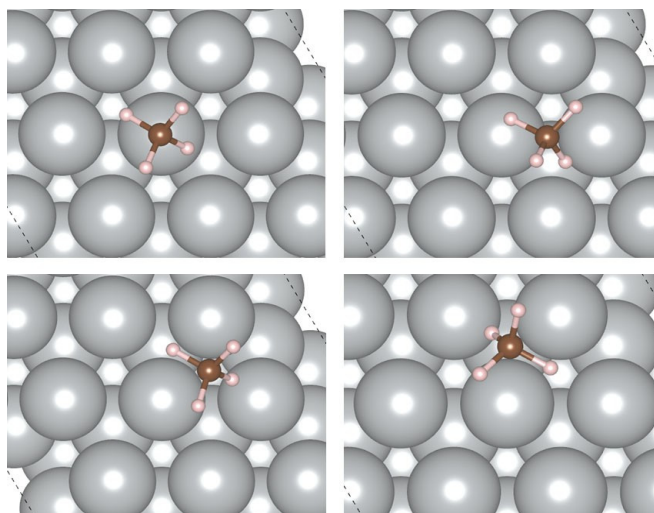
Figure 4. Atomic geometries of methane adsorption in different sites as calculated in the (4 × 4) unit cell of the clean Ni(111) surface. Upper left to right: on-top and bridge; lower left to right: fcc-hollow site and hcp-hollow site.

Table 3. Adsorption energies for CH_4 and the dissociation reaction intermediates on the Ni(111) surface for two different coverages (1/16 and 1/4 ML), as calculated in the (4 × 4) and (2 × 2) surface unit cells, respectively. Also shown are the adsorption energies for the presence of subsurface C, E^{sub}, as calculated in the (4 × 4) surface unit cell. The relative energy differences, with and without subsurface C, ΔE^{sub}, and for using a (4 × 4) and (2 × 2) surface unit cell, ΔE, are also listed.

Site	(4 × 4) E_{ads} (eV)	E^{sub} (eV)	ΔE^{sub} (eV)	(2 × 2) E_{ads} (eV)	ΔE (eV)
CH_4 on-top	−0.15	−0.16			
CH_4 bridge	−0.15				
CH_4 fcc	−0.14				
CH_4 hcp	−0.14				
CH_3 fcc	−2.61	−2.16	0.44	−2.51	0.10
CH_3 hcp	−2.06	−2.06	0.00	−2.51	−0.45
CH_3 top	−2.18	−2.17	0.01	−2.17	0.02
CH_2 fcc	−4.35	−3.65	0.70	−4.36	−0.01
CH_2 hcp	−4.30	−4.11	0.20	−4.33	−0.02
CH_2 top	−3.27	−3.10	0.17	−4.36	−1.09
CH fcc	−6.68	−5.76	0.92	−6.62	0.05
CH hcp	−6.67	−6.34	0.31	−6.65	0.02
CH top	−6.64	−6.20	0.44	−6.62	0.01
H fcc	−2.99	−2.56	0.43	−2.93	0.05
H hcp	−2.95	−2.86	0.10	−2.40	0.55
H top	−2.37	−2.31	0.06	−1.93	0.44
C fcc	−7.05	−6.13	0.93	−7.06	−0.01
C hcp	−7.14	−6.80	0.34	−7.13	0.01
C top	−4.85	−4.47	0.37	−4.78	0.07
C Subsurface octa	−7.79			−7.57	0.23
C Subsurface tetra	−7.14			−6.15	0.99

The results for the adsorption energies of the intermediates on the Ni(111) surface are shown in Table 3, along with those for the presence of subsurface C. CH_3 has an adsorption energy of −2.61 eV, while CH_2 is substantially stronger, with −4.35 eV. The strongest adsorbed intermediate is CH, with −6.68 eV.

It can be seen from Table 3 that for the low coverage of adsorbates calculated in the (4×4) surface unit cell, for CH_3, CH_2, CH, and H, the most favourable site is the fcc-hollow site. Compared to available experimental values, good agreement of the calculated adsorption energy of CH_3 (-2.61 eV, fcc) with the experimental value of -2.26 eV in the fcc site, as obtained through calorimetry [38], is obtained.

As discussed above, for the adsorption of on-surface C, the most favourable site is the hcp-hollow site. The effect of the presence of subsurface C (placed in the octahedral site, below the fcc-hollow site, and bonded above to a surface Ni atom that the intermediates also bond to) notably weakens the bonding of the on-surface adparticles by values ranging from 0.01 to 0.92 eV. The most significant effect is for adsorption in the fcc site, because here the subsurface C atom is located directly below the adparticle. For some cases, this causes the hcp site to become more favourable (i.e., for CH_2, CH, C, and H). Correspondingly, subsurface C induces a lengthening of the molecule-Ni bond-length. This is illustrated in Figures S6 and S7 for methane and CH_3, respectively. For methane, the bond-length has increased from 2.407 to 2.591 Å (difference of 0.184 Å) with the presence of subsurface C, consistent with the weaker adsorption energy. Similarly, as shown in Figure S7, the average distances between CH_3 and the three closest nickel atoms has increased from 2.10 Å for the clean Ni(111) surface to 2.134 Å for that with subsurface carbon.

The effect of adsorbate coverage is also investigated by carrying out analogous calculations using a smaller (2×2) surface unit cell, corresponding to a coverage of 0.25 ML, which is four times the coverage of that $(1/16 = 0.0625$ ML) when calculated in the (4×4) surface unit cell. The results for 0.25 ML are listed in Table 3, which show that for most cases, the fcc-hollow site is still the most favourable, or they are degenerate with the hcp-hollow site (CH_3) or the on-top site (CH_2), with the exception of CH, where the hcp-hollow is the most favourable, but only by 0.03 eV. These values can be compared with the ab initio calculations of Wang et al. [4], Zhu et al. [39], and Wang et al. [40], where, largely, the same preferred adsorption sites and trends were reported.

4.2. Adsorption on the SAA Surfaces

We now turn to consider the adsorption of methane and intermediates on the single-atom alloy surfaces, and the adsorption energies are listed in Table 4. These are created by substitutionally adsorbing different metal atoms in the Ni(111) surface; specifically, Cu, Fe, Pt, Pd, Zn, and Al are considered. We find that the Ni atoms exhibit a magnetization of between 0.65 and 0.71 μ_B and that the non-magnetic atoms acquire a small magnetization of less than 0.25 μ_B, while Fe has a substantial value of 2.95 μ_B. The doped atoms further bind exothermically into the host material and hybridize with the Ni states (see, e.g., Figure S9).

Table 4. Adsorption energies (eV) for CH_4 and the dissociation reaction intermediates on the (4×4) unit cell of Ni (111) with different single doping of metal atoms.

Adsorbates	Cu	Fe	Pt	Pd	Zn	Al	Ni
CH_4	−0.18	−0.17	−0.19	−0.20	−0.19	−0.20	−0.15
CH_3	−2.33	2.5	−2.24	−2.31	−2.15	−2.53	−2.61
CH_2	−4.02	−3.95	−4.22	−3.98	−3.86	−3.97	−4.35
CH	−6.18	−6.45	−6.46	−6.35	−6.57	−6.57	−6.68
C	−5.63	−9.75	−8.31	−6.98	−3.74	−7.14	−7.14

For the adsorption of methane, the SAA structures strengthen the adsorption energy relative to the Ni(111) surface by 0.03, 0.02, 0.04, 0.05, 0.04, and 0.05 eV for Cu, Fe, Pt, Pd, Zn, and Al, respectively. The adsorption strength of the $CH_x(x = 1, 3)$ fragments are much stronger than methane, with values ranging from −2.61 eV (Ni(111)) to −2.15 eV (Zn-SAA) for CH_3. For CH_2, the strongest adsorption energy is −4.22 eV for Pt-SAA, followed by −4.02 eV for the Cu-SAA. The adsorption energy of CH is greatest for Ni(111) (−6.68 eV), followed by Al- and Zn-SAA, both with −6.57 eV. For C, the adsorption energies

are generally stronger (-9.75 eV for Fe to -6.98 eV for Pd), with the exception of Cu (-5.63 eV) and Zn (-3.74 eV). These two latter systems have full *d*-bands for the doped atom, explaining the smaller values.

5. Methane Decomposition

We now determine the reaction barriers for methane decomposition. The four reaction pathways are:

$$CH_4 \rightarrow CH_3 + H \tag{4}$$

$$CH_3 \rightarrow CH_2 + H \tag{5}$$

$$CH_2 \rightarrow CH + H \tag{6}$$

$$CH \rightarrow C + H \tag{7}$$

It is interesting to first consider the energy cost to remove one hydrogen from methane in the gas phase. We did this both by manually increasing the distance between the C atom of CH_4 and one of the H atoms, as well as through the NEB climbing image method. As shown in Figure S8, the NEB calculation gives a smooth reaction curve and a barrier energy of 5.3 eV at 1.37 Å. The manual result gives a similar barrier of around 5.4 eV at a distance of 1.15 Å from the initial H position. The barrier is clearly significant and much greater than over a catalyst surface as expected, as we shall see below.

5.1. Methane Decomposition: Over Ni(111) and $C_{subsurf}$/Ni(111)

In the following section, we first investigate the dehydrogenation of methane over the Ni(111) surface compared to the results of previous ab initio calculations and how the behaviour changes with the presence of subsurface carbon at 0.25 ML positioned in the octahedral site under the first layer. For the clean Ni(111) surface, in Figures 5–8, the initial, final, and transition state geometries for the decomposition of methane are displayed. The corresponding reaction pathway and barriers are shown in Figure 9, and the barrier heights are listed in Table 5. In the reaction energy diagrams (Figures 9 and 10), we do not include the zero-point energy nor vibrational entropy because our focus is on trends, and because the systems are very similar, we expect very similar values for these contributions.
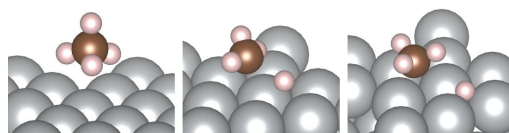
Figure 5. Atomic geometry along the reaction path $CH_4 \rightarrow CH_3 + H$ (from left to right) using a (4×4) surface unit cell of the Ni(111) surface.
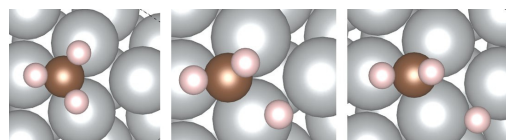

Figure 6. Atomic geometry along the reaction path $CH_3 \rightarrow CH_2 + H$ (from left to right) using a (4×4) surface unit cell of the Ni(111) surface.
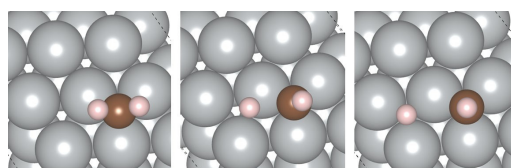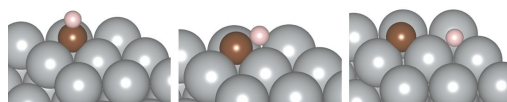

Figure 7. Atomic geometry along the reaction path $CH_2 \rightarrow CH + H$ (from left to right) using a (4×4) surface unit cell of the Ni(111) surface.

Figure 8. Atomic geometry along the reaction path CH → C + H (from left to right) using a (4 ×4) surface unit cell of the Ni(111) surface.
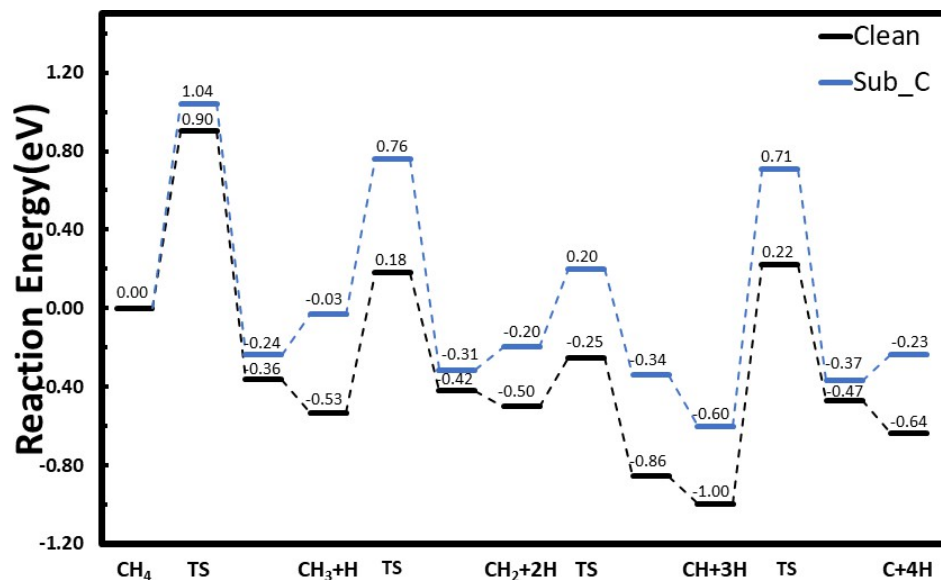

Figure 9. Energies along the reaction pathway for CH$_4$ dissociation over the clean Ni(111) surface and the Ni(111) surface with 0.25 ML subsurface C atoms under the first layer in the octahedral site, where "TS" represents the transition state for the reaction activation energy barrier. The energy level to the right of the transition state is the final state from the NEB calculation, and the level to the right of this is where the dissociated H atom has diffused to an isolated position on the Ni(111) surface.
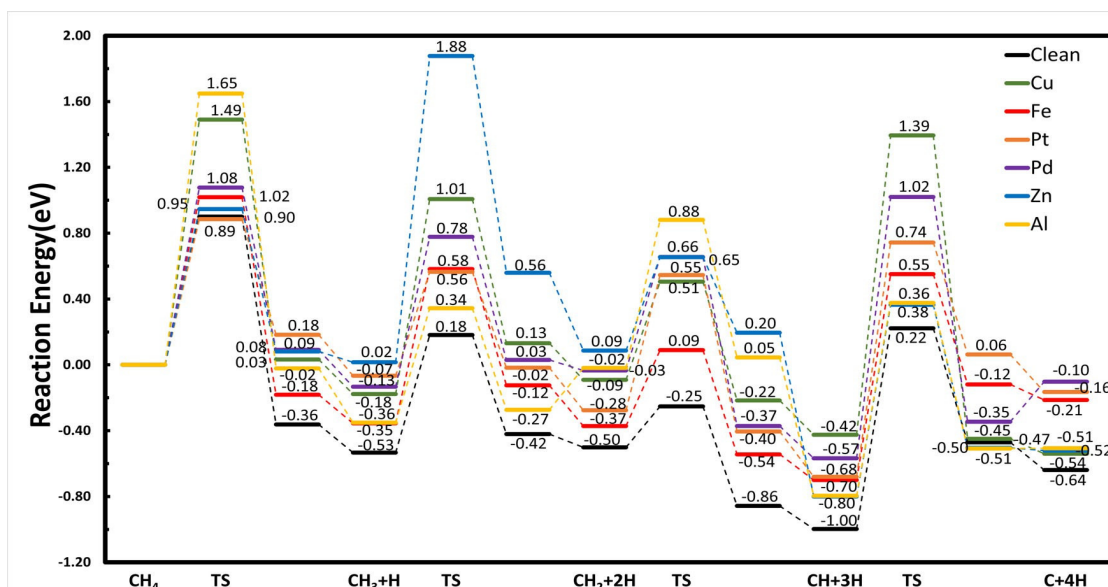
Figure 10. Energies along the reaction pathway for methane dissociation over the various single-atom alloy surfaces. "TS" represents the transition state for the associated reaction activation energy barrier. The energy level to the right of the transition state is the final state from the NEB calculation, and the level to the right of this is where the dissociated H atom has diffused to an isolated position on the Ni(111) surface.

Table 5. Reaction barrier energies (eV) for methane decomposition over the Ni(111) and SAA surfaces.

Reaction Barriers	Cu	Fe	Pt	Pd	Zn	Al	Ni	$C_{subsurf}$/Ni
$CH_4 \rightarrow CH_3 + H$	1.49	1.02	0.89	1.08	0.95	1.65	0.90	1.04
$CH_3 \rightarrow CH_2 + H$	1.19	0.94	0.63	0.91	1.86	0.70	0.71	0.79
$CH_2 \rightarrow CH + H$	0.60	0.46	0.82	0.69	0.57	0.90	0.25	0.40
$CH \rightarrow C + H$	1.82	1.26	1.43	1.59	1.16	1.17	1.22	1.31

The first to fourth H removal steps have associated reaction barriers of 0.90 eV, 0.71 eV, 0.25 eV, and 1.22 eV, respectively. We can compare these values with previous results in the literature. Liu et al. [41] performed investigations into methane dehydrogenation over NiCu surfaces where the reaction energy barriers were reported. Their study used the Cambridge Sequential Total Energy Package (CASTEP), also with the GGA-PBE functional, where four different systems were considered, namely, methane dehydrogenation over Ni(111), Cu(111), and two different NiCu(111) surfaces. For the reaction over the Ni(111) surface, the activation energies of the four steps of methane dehydrogenation were reported to be 1.18 eV, 0.77 eV, 0.37 eV, and 1.36 eV. These values are slightly higher than the present results, which could be due to the smaller simulation cell consisting of three metal layers and a (2×2) surface unit cell.

In another DFT study [42], the dry reforming of methane (DRM) over Ni, Pd, and Pt surfaces was investigated. The calculations were performed using VASP with the GGA for the exchange-correlation functional. The reported energy barriers of the methane dehydrogenation steps over Ni(111) were 2.342 eV, 0.56 eV, 0.29 eV, and 1.223 eV, where clearly the activation energy of the first step is significantly higher than that of the present work and that of [41]. One difference is that this study took into account the effect of temperature, assuming a temperature of 973.15 K.

It is apparent that the first reaction step of removing one hydrogen atom from methane has the highest barrier, with other values in the literature reported to be 1.41 eV [39], 1.04 eV [43], 1.32 eV [44], and 1.12 eV [45].

In calculating the reaction energy diagrams in Figures 9 and 10, we show the energy position of the relative initial state, the transition state, and the final state, as well as where the dissociated H atom has diffused to an isolated position on the Ni(111) surface. This latter step is important to ensure that the interaction between the dissociated H atom and the associated fragment does not influence the initial state of the next reaction step. It also conserves the total number of atoms at every step and has a common energy reference, as depicted in Figure S10. Not considering this H diffusion step results in somewhat different energy profiles, as shown in Figures S11 and S12.

It is interesting to consider the effect of subsurface C on the reaction energy barriers for methane dehydrogenation on Ni(111). We found that subsurface C increases the reaction barriers and reduces the adsorption energies of the intermediates for all reaction steps, thus reducing the performance of Ni(111). For example, it can be seen from Figure 9 that for $CH_4 \rightarrow CH_3 + H$, the presence of subsurface carbon yields an increase in the reaction energy barrier relative to that of the clean Ni(111) surface of 0.14 eV, namely, the barrier is 1.04 eV compared to 0.90 eV. A similar increase in the activation barrier for subsequent hydrogen removal steps can be seen from Figure 9 and from Table 5, i.e., there are increases of 0.08, 0.15, and 0.09 eV for CH_3, CH_2, and CH dehydrogenation, respectively.

Interestingly, Arevalo et al. [46] reported that on stepped nickel surfaces, subsurface carbon atoms that formed specific Ni-C structures at the step edge improved the selectivity toward methane decomposition. This site was characterized by a fivefold-coordinated bonding of C with Ni atoms. These results, and the present ones, indicate that the reaction is sensitive to the specific Ni-C local geometry.

5.2. Methane Decomposition over the SAA Surfaces

We now turn to consider the SAA surfaces. The calculated reaction energy diagram is shown in Figure 10. It can be seen that the activation energy for removing the first hydrogen atom from methane is lowest for Pt-SAA (0.89 eV), followed by clean Ni(111). The barrier for the Zn-SAA surface is only slightly greater than for Ni(111), with a value of 0.95 eV. Fe- and Pd-SAA surfaces have similar barriers of 1.02 and 1.08 eV, respectively, while Cu- and Al-SAA surfaces have the highest barriers, with 1.49 and 1.65 eV, respectively.

For the second dehydrogenation step, $CH_3 \rightarrow CH_2 + H$, the lowest barrier is again for Pt-SAA (0.63 eV), followed by Al-SAA, with 0.70 eV. The Ni(111) surface has the next lowest reaction barrier at 0.71 eV, while other structures have barriers greater than 0.9 eV.

The third dehydrogenation step, $CH_2 \rightarrow CH$, has a very low barrier of 0.25 eV for the reaction over the Ni(111) surface. Also with a low barrier is the reaction over Fe-SAA (0.46 eV), closely followed by Zn- and Cu-SAA, with 0.57 and 0.60 eV, respectively. The remaining barriers are higher; in increasing order, they are 0.69, 0.82, and 0.90 eV for Pd-, Pt-, and Al-SAA, respectively.

The final reaction step, in which the CH bond is split into an adsorbed C and H atom, has a high barrier for all surfaces. The lowest is for Zn- and Al-SAA, with barriers of 1.16 and 1.17 eV, respectively, and the next lowest are the clean Ni(111) and Fe-SAA, with 1.22 and 1.25 eV, respectively. The highest barriers are for Pt-, Pd-, and Cu-SAA, with values of 1.43, 1.59, and 1.82 eV, respectively. These results suggest that doping the Ni(111) surface with both Al or Zn atoms and Pt atoms, functioning as distinct active sites, could result in improved reactivity and/or selectivity for methane decomposition.

5.3. d-Band Centre

It is well-known that in many cases, the reaction barrier scales roughly linearly with the energy of the *d*-band centre (see Ref. [47] and references therein). It is therefore of interest to see if there is a correlation between the present activation barriers and the *d*-band centre. From Figure 11 [48], it can be seen that there is a general correlation amongst some of the surfaces, but there are also some exceptions. Considering, for example, Fe-, Pd-, and Cu-SAA, one can see there is a direct correlation between increasing the barrier and decreasing (such that it is more negative and further away from the Fermi level) the *d*-band centre position. Ni- and Pt-SAA are exceptions because they display a sharp dip in the reaction barrier energy (i.e., lower). Zinc does not fit the trend of increasing reaction barrier with decreasing *d*-band centre due to the zinc atom having a full *d*-band as well as a fully occupied *s* state. In particular, with the exception of CH_3 dehydrogenation, it yields a distinct lowering of the reaction barrier relative to Cu, and in some cases even to Pt (CH and CH_2 dehydrogenation).
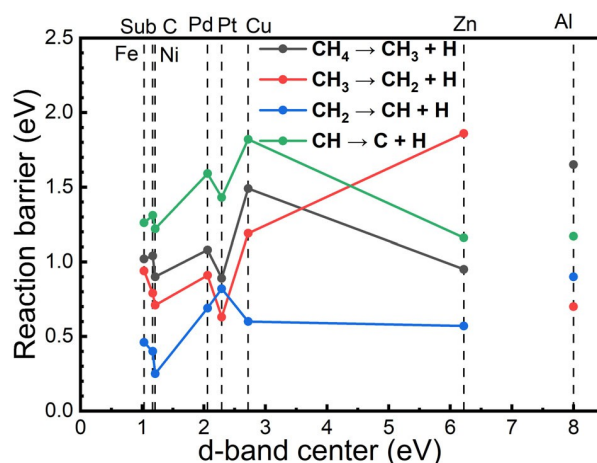
Figure 11. Reaction barrier plotted against the position of the *d*-band centre for the surfaces considered. For Al, due to the lack of a valence *d*-state, the reaction barriers are plotted at an arbitrary value of 8 eV.

6. Conclusions

We performed DFT calculations to investigate the activity for methane decomposition of a series of single-atom alloys (SAAs) created through the substitution of Cu, Fe, Pt, Pd, Zn, and Al atoms into the surface layer of Ni(111). For the adsorption of carbon on Ni(111), the adsorption energy of on-surface homogeneously dispersed C atoms is less favourable than the subsurface adsorption of C atoms under the first Ni layer. The formation of graphene on the surface is, however, the most favourable, which is consistent with experimental observations of graphtic carbon at elevated temperatures. For methane decomposition, our results show that the presence of subsurface carbon reduces the stability and activity of the reaction intermediates, increases the reaction barriers, and reduces the adsorption energies, thereby lowering the performance of the Ni(111) catalyst. On the other hand, Al-, Zn-, and Pt-SAAs are found to reduce the barriers for the $CH_4 \rightarrow CH_3 + H$ and $CH_3 \rightarrow CH_2 + H$ (Pt) reactions, as well as for the $CH \rightarrow C + H$ (Al, Zn) reaction. Clean Ni(111) yields the lowest barrier for $CH_2 \rightarrow CH + H$. These findings suggest that doping the Ni surface with both or either Al and Zn atoms and Pt atoms, functioning as distinct active sites, may bring about improved activity and/or selectivity for methane decomposition.

References

1. Abbas, H.F.; Daud, W.M.W. Hydrogen production by methane decomposition: A review. *Int. J. Hydrogen Energy* **2010**, *35*, 1160–1190. [CrossRef]
2. Sánchez-Bastardo, N.; Schlogl, R.; Ruland, H. Methane pyrolysis for zeroemission hydrogen production: A potential bridge technology from fossil fuels to a renewable and sustainable hydrogen economy. *Ind. Eng. Chem. Res.* **2021**, *60*, 11855–11881. [CrossRef]
3. Hasnan, N.S.N.; Timmiati, S.N.; Lim, K.L.; Yaakob, Z.; Kamaruddin, N.H.N.; Teh, L.P. Recent developments in methane decomposition over heterogeneous catalysts: An overview. *Mater. Renew. Sustain. Energy* **2020**, *9*, 1–18. [CrossRef]
4. Wang, S.-G.; Cao, D.-B.; Li, Y.-W.; Wang, J.; Jiao, H. Co₂ re-forming of ch₄ on ni(111): A density functional theory calculation. *J. Phys. Chem. B* **2006**, *110*, 9976–9983. [CrossRef]

5. Minh, D.P.; Siang, T.J.; Vo, D.-V.N.; Phan, T.S.; Ridart, C.; Nzihou, A.; Grouset, D. Hydrogen production from biogas reforming: An overview of steam reforming, dry reforming, dual reforming, and tri-reforming of methane. *Hydrogen Supply Chain.* **2018**, 111–166.
6. Nair, M.M.; Kaliaguine, S. Structured catalysts for dry reforming of methane. *New J. Chem.* **2016**, *40*, 4049–4060. [CrossRef]
7. Pakhare, D.; Spivey, J. A review of dry (CO_2) reforming of methane over noble metal catalysts. *Chem. Soc. Rev.* **2014**, *43*, 7813–7837. [CrossRef] [PubMed]
8. Hannagan, R.T.; Giannakakis, G.; Flytzani-Stephanopoulos, M.; Sykes, E.C.H. Single-atom alloy catalysis. *Chem. Rev.* **2020**, *120*, 12044–12088. [CrossRef] [PubMed]
9. Zhang, T.; Walsh, A.G.; Yu, J.; Zhang, P. Single-atom alloy catalysts: Structural analysis, electronic properties and catalytic activities. *Chem. Soc. Rev.* **2021**, *50*, 569–588. [CrossRef] [PubMed]
10. Greiner, M.T.; Jones, T.E.; Beeg, S.; Zwiener, L.; Scherzer, M.; Girgsdies, F.; Piccinin, S.; Armbru, M.; Knop-Gericke, A.; Schl, R. Free-atom-like d states in single-atom alloy catalysts. *Nat. Chem.* **2018**, *10*, 1008–1015. [CrossRef] [PubMed]
11. Liu, J.; Lucci, F.R.; Yang, M.; Lee, S.; Marcinkowski, M.D.; Therrien, A.J.; Williams, C.T.; Sykes, E.C.H.; Flytzani-Stephanopoulos, M. Tackling co poisoning with single-atom alloy catalysts. *J. Am. Chem. Soc.* **2016**, *138*, 6396–6399. [CrossRef] [PubMed]
12. Kyriakou, G.; Boucher, M.B.; Jewell, A.D.; Lewis, E.A.; Lawton, T.J.; Baber, A.E.; Tierney, H.L.; Flytzani-Stephanopoulos, M.; Sykes, E.C.H. Isolated metal atom geometries as a strategy for selective heterogeneous hydrogenations. *Science* **2012**, *335*, 1209–1212. [CrossRef] [PubMed]
13. Alves, L.; Pereira, V.; Lagarteira, T.; Mendes, A. Catalytic methane decomposition to boost the energy transition: Scientific and technological advancements. *Renew. Sustain. Energy Rev.* **2021**, *137*, 110465. [CrossRef]
14. Ali, S.; Zagho, M.M.; Al-Marri, M.J.; Arafat, Y.I.; Khader, M.M. Development of nickel-based catalysts for methane steam reforming. In Proceedings of the 4th International Gas Processing Symposium, Doha, Qatar, 26–27 October 2014; Elsevier: Amsterdam, The Netherlands, 2015; pp. 111–116.
15. Hafner, J.; Kresse, G. The vienna ab-initio simulation program vasp: An efficient and versatile tool for studying the structural, dynamic, and electronic properties of materials. *Prop. Complex Inorg. Solids* **1997**, *6982*, 69–82.
16. Perdew, J.P.; Burke, K.; Ernzerhof, M. Generalized gradient approximation made simple. *Phys. Rev. Lett.* **1996**, *77*, 38653868. [CrossRef] [PubMed]
17. Grimme, S.; Antony, J.; Ehrlich, S.; Krieg, H. A consistent and accurate ab initio parametrization of density functional dispersion correction (dft-d) for the 94 elements h-pu. *J. Chem. Phys.* **2010**, *132*, 154104. [CrossRef] [PubMed]
18. Monkhorst, H.J.; Pack, J.D. Special points for brillouin-zone integrations. *Phys. Rev. B* **1976**, *13*, 51885192. [CrossRef]
19. Henkelman, G.; Uberuaga, B.P.; Jnsson, H. A climbing image nudged elastic band method for finding saddle points and minimum energy paths. *J. Chem. Phys.* **2000**, *113*, 99019904. [CrossRef]
20. Henkelman, G.; Jnsson, H. Improved tangent estimate in the nudged elastic band method for finding minimum energy paths and saddle points. *J. Chem. Phys.* **2000**, *113*, 99789985. [CrossRef]
21. Engelmann, Y.; Bogaerts, A.; Neyts, E.C. Thermodynamics at the nanoscale: Phase diagrams of nickel-carbon nanoclusters and equilibrium constants for phase transitions. *Nanoscale* **2014**, *6*, 1198111987. [CrossRef]
22. Caldero, L.A.; Montoya, A.; Soon, A.; Stamp, C. Non-dissociative adsorption of glycerol on the (111) surface of ni and pt-based metallic systems: Hints on re- forming activity from *d*-band center. *Mol. Catal.* **2019**, *474*, 110412. [CrossRef]
23. Du, P.; Wu, P.; Cai, C. Mechanistic insight into the facet-dependent adsorption of methanol on a pt₃ni nanocatalyst. *J. Phys. Chem. C* **2015**, *119*, 18352–18363. [CrossRef]
24. Janthon, P.; Luo, S.; Kozlov, S.M.; Vines, F.; Limtrakul, J.; Truhlar, D.G.; Illas, F. Bulk properties of transition metals: A challenge for the design of universal density functionals. *J. Chem. Theory Comput.* **2014**, *10*, 3832–3839. [CrossRef]
25. Lejaeghere, K.; Van Speybroeck, V.; Van Oost, G.; Cottenier, S. Error estimates for solid-state density-functional theory predictions: An overview by means of the ground-state elemental crystals. *Crit. Rev. Solid State Mater. Sci.* **2014**, *39*, 1–24. [CrossRef]
26. Klinke, D.J., II; Wilke, S.; Broadbelt, L.J. A theoretical study of carbon chemisorption on ni (111) and co (0001) surfaces. *J. Catal.* **1998**, *178*, 540–554. [CrossRef]
27. Zhang, Q.-M.; Wells, J.C.; Gong, X.G.; Zhang, Z. Adsorption of a carbon atom on the ni 38 magic cluster and three low-index nickel surfaces: A comparative first-principles study. *Phys. Rev. B* **2004**, *69*, 205413. [CrossRef]
28. Haynes, W.M. (Ed.) *CRC Handbook of Chemistry and Physics*; Properties of solids; CRC Press: Boca Raton, FL, USA, 2014; Chapter 12; p. 124.
29. Michaelson, H.B. The work function of the elements and its periodicity. *J. Appl. Phys.* **1977**, *48*, 47294733. [CrossRef]
30. Shi, H.; Stamp, C. Shape and surface structure of gold nanoparticles under oxidizing conditions. *Phys. Rev. B* **2008**, *77*, 094127. [CrossRef]
31. Soon, A.; Wong, L.; Delley, B.; Stamp, C. Morphology of copper nanoparticles in a nitrogen atmosphere: A first-principles investigation. *Phys. Rev. B* **2008**, *77*, 125423. [CrossRef]
32. Sche, M.; Stamp, C.; Horn, E.K. Handbook of surface science. In *Electronic Structure*; Elsevier: Amsterdam, The Netherlands, 2000; Volume 2, pp. 286–356.
33. Klink, C.; Stensgaard, I.; Besenbacher, F.; Lægsgaard, E. An stm study of carbon-induced structures on ni (111): Evidence for a carbidic-phase clock reconstruction. *Surf. Sci.* **1995**, *342*, 250–260. [CrossRef]

34. Gardin, D.E.; Batteas, J.D.; Van Hove, M.A.; Somorjai, G.A. Carbon, nitrogen, and sulfur on ni (111): Formation of complex structures and consequences for molecular decomposition. *Surf. Sci.* **1993**, *296*, 25–35. [CrossRef]

35. Grimme, S.; Ehrlich, S.; Goerigk, L. Effect of the damping function in dispersion corrected density functional theory. *J. Comput. Chem.* **2011**, *32*, 14561465. [CrossRef]

36. Dion, M.; Rydberg, H.; Schr, E.; Langreth, D.C.; Lundqvist, B.I. Van der waals density functional for general geometries. *Phys. Rev. Lett.* **2004**, *92*, 246401. [CrossRef]

37. Niu, J.; Ran, J.; Du, X.; Qi, W.; Zhang, P.; Yang, L. Effect of pt addition on resistance to carbon formation of ni catalysts in methane dehydrogenation over ni-pt bimetallic surfaces: A density functional theory study. *Mol. Catal.* **2017**, *434*, 206–218. [CrossRef]

38. Carey, S.J.; Zhao, W.; Frehner, A.; Campbell, C.T.; Jackson, B. Energetics of adsorbed methyl and methyl iodide on ni (111) by calorimetry: Comparison to pt (111) and implications for catalysis. *ACS Catal.* **2017**, *7*, 1286–1294. [CrossRef]

39. Zhu, Y.-A.; Chen, D.; Zhou, X.-G.; Yuan, W.-K. Dft studies of dry reforming of methane on ni catalyst. *Catal. Today* **2009**, *148*, 260–267. [CrossRef]

40. Wang, X.; Yuan, Q.; Li, J.; Ding, F. The transition metal surface dependent methane decomposition in graphene chemical vapor deposition growth. *Nanoscale* **2017**, *9*, 11584–11589. [CrossRef] [PubMed]

41. Liu, H.; Zhang, R.; Yan, R.; Li, J.; Wang, B.; Xie, K. In- sight into ch4 dissociation on nicu catalyst: A first-principles study. *Appl. Surf. Sci.* **2012**, *258*, 81778184. [CrossRef]

42. Foppa, L.; Silaghi, M.-C.; Larmier, K.; Comas-Vives, A. Intrinsic reactivity of ni, pd and pt surfaces in dry reforming and competitive reactions: Insights from first principles calculations and microkinetic modeling simulations. *J. Catal.* **2016**, *343*, 196207. [CrossRef]

43. Bengaard, H.S.; Nrskov, J.K.; Sehested, J.; Clausen, B.S.; Nielsen, L.P.; Molenbroek, A.M.; Rostrup-Nielsen, J.R. Steam reforming and graphite formation on ni catalysts. *J. Catal.* **2002**, *209*, 365384. [CrossRef]

44. Watwe, R.M.; Bengaard, H.S.; Rostrup-Nielsen, J.R.; Dumesic, J.A.; Norskov, J.K. Theoretical studies of stability and reactivity of chx species on ni(111). *J. Catal.* **2000**, *189*, 1630. [CrossRef]

45. Kratzer, P.; Hammer, B.; Norskov, J.K. A theoretical study of ch$_4$ dissociation on pure and goldalloyed ni(111) surfaces. *J. Chem. Phys.* **1996**, *105*, 55955604. [CrossRef]

46. Arevalo, R.L.; Aspera, S.M.; Escao, M.C.; Nakanishi, H.; Kasai, H. Tuning methane decomposition on stepped ni surface: The role of subsurface atoms in catalyst design. *Sci. Rep.* **2017**, *7*, 13963. [CrossRef] [PubMed]

47. Abild-Pedersen, F.; Greeley, J.; Nørskov, J.K. Understanding the effect of steps, strain, poisons, and alloying: Methane activation on ni surfaces. *Catal. Lett.* **2005**, *105*, 9–13. [CrossRef]

48. The d-Band Center Is Calculated Using the Perl Script Called dosanalyze.pl. Github Site of Raghvender. Available online: https://github.com/rvraghvender/VASP-codes (accessed on 8 February 2024).